

Imaging the geometrical structure of complex symmetric molecules by above-threshold ionization spectrum in an IR+XUV laser field

Xu-Cong Zhou^{1,2}, Shang Shi^{1,8}, Fei Li^{1,8}, Ying-Chun Guo³, Yu-Jun Yang⁴, Qing-Tian Meng², Jing Chen^{5,6}, Xiao-Jun Liu⁷ and Bingbing Wang^{1,8,[✉]}

¹*Laboratory of Optical Physics, Beijing National Laboratory for Condensed Matter Physics, Institute of Physics, Chinese Academy of Sciences, Beijing 100190, China*

²*School of Physics and Electronics, Shandong Normal University, Jinan 250358, China*

³*Department of Physics, School of Physics and Electronics, East China Normal University, Shanghai 200062, China*

⁴*Institute of Atomic and Molecular Physics, Jilin University, Changchun 130012, China*

⁵*HEDPS, Center for Applied Physics and Technology, Peking University, Beijing 100871, China*

⁶*Institute of Applied Physics and Computational Mathematics, Beijing 100088, China*

⁷*State Key Laboratory of Magnetic Resonance and Atomic and Molecular Physics, Wuhan Institute of Physics and Mathematics, Chinese Academy of Sciences, Wuhan 430071, China*

⁸*University of Chinese Academy of Sciences, Beijing 100049, China*

Based on the frequency-domain theory, we put forward a method of imaging the complex symmetrical polyatomic molecules by using IR+XUV two-color laser fields. Although the wave function of a polyatomic molecule, such as SF₆, is quite complex in momentum space, it can be simplified by several terms in the region of high value of momentum, where the destructive interference fringes from these terms carry the information of the molecular structure. In this work, we find that, since the XUV laser field may increase the kinetic energy of the

[✉]wbb@aphy.iphy.ac.cn

photoelectron dramatically in the above-threshold ionization (ATI) process of a molecule in an IR+XUV two-color laser field, the information of the molecular structure can be obtained by analyzing the interference fringes of the ATI spectrum in the high-energy region, where the simplified wave function of the molecule plays a dominant role in this part of the ATI spectrum. This method provides a unique accessible route towards imaging polyatomic molecules from a frequency perspective.

I. INTRODUCTION

The emergence of strong laser fields has revealed many new nonlinear physical phenomena. One of the most important processes is above threshold ionization (ATI) [1-3], which was first found in forty years ago. As a direct photoionization process, ATI spectrum has been widely used in deriving the information of the molecular structures [4-5] and observing the dynamic processes of molecules in laser fields [6-7]. Later on, re-collision processes [8] in strong laser field, such as high-order above-threshold ionization (HATI) process [9-11] and high harmonic generation (HHG) [12-13], were observed. Therefore, in the re-collision process, the ionized electron driven by the reverse laser field has a certain probability to re-collide with the nuclei, so as to form fringes by interference between different re-collision paths carrying related molecular structure information in the electron energy spectrum [14-17]

or harmonic spectrum [18-19]. However, for heteronuclear diatomic molecules [20], the ionized electron can only re-collide with the nucleus carrying positive charge, hence it is hard to accurately image the corresponding molecular structure by these re-collision spectra.

Recently, with the development of high frequency laser technique by high-order harmonic generation and free-electron laser, the pump-probe method becomes an effective tool to measure and control the ultrafast dynamic processes in the laser-matter interactions [21-27]. Especially, the ionization and dissociation of molecules can be observed and controlled by changing the laser conditions and the delay time between the two laser pulses [22-27]. For example, the lifetime of the charge-transfer processes in Argon dimers has been obtained by XUV+IR pump-probe experiments [24]. More recently, He *et al.* [21] demonstrated that the orientation- and molecular-orbital-resolved ionization can be used to retrieve the complex structure of molecules by controlling the intensity of two-color laser fields. However, since many electronic orbitals may participate in the pump-probe dynamic processes for complex molecules, it is still a tough task to derive the information of the molecular structure by analyzing the experimental data [28].

What discussed above is mainly based on time-domain investigation in coordinate space, and they are time consuming even if it can reflect the molecular structure information to some extent. In this work, we employ

the frequency-domain theory based on a non-perturbative quantum electrodynamics, which has previously been used to handle problems related to strong fields [29-33], to deal with the angle-resolved ATI spectra of complex molecules in linearly polarized IR+XUV two-color laser fields. The purpose of using the two-color laser fields is to get a broad energy spectrum, where IR laser can broaden the spectrum and XUV laser can help us obtain high ionization probability of the electron in the molecule, which is beneficial to extract the complex molecular structural information. The research object here is the complex polyatomic molecule with high symmetry, *i.e.*, SF₆. We find that the molecular states in momentum space can be simplified in high energy region, and many interference formulas carrying the information of the bond lengths may be obtained by these simplified states. Therefore, the interference fringes in ATI spectrum can be used to predict the bond lengths by the corresponding interference formulas.

II. THEORETICAL METHOD

In this work, we consider the ATI process of one polyatomic molecule in IR+XUV two-color laser fields. The frequency-domain representation of the method for ATI in two-color laser fields is given in [32-33]. Here this method is briefly summarized and applied for polyatomic molecule system. Based on the frequency-domain theory, the

Hamiltonian of the molecule-laser system can be written as

$$H = H_0 + U + V, \quad (1)$$

where $H_0 = \frac{(-i\nabla)^2}{2m_e} + \omega_1 N_{a_1} + \omega_2 N_{a_2}$ represents the energy operator for a free electron-photon system, $N_{a_i} = \frac{1}{2}(a_i^\dagger a_i + a_i a_i^\dagger)$ is the photon number operator of the laser field with frequency ω_i , where a_i and a_i^\dagger are the annihilation operator and creation operator of the photon mode for $i=1, 2$. U represents the molecular binding potential, and V is the electron-photon interaction potential expressed by

$$V = -\frac{e}{2m_e} \{(-i\nabla) \cdot [\mathbf{A}_1(\mathbf{r}) + \mathbf{A}_2(\mathbf{r})] + [\mathbf{A}_1(\mathbf{r}) + \mathbf{A}_2(\mathbf{r})] \cdot (-i\nabla)\} + \frac{e^2}{2m_e} [\mathbf{A}_1(\mathbf{r})^2 + \mathbf{A}_2(\mathbf{r})^2], \quad (2)$$

where $\mathbf{A}_s(\mathbf{r}) = g_s (\hat{\mathbf{e}}_s e^{i\mathbf{k}\cdot\mathbf{r}} a_s + c.c.)$ is the vector potential with $g_s = (2\omega_s V_\gamma)^{-1/2}$ ($s=1,2$) and V_γ is the normalized volume of the laser field.

The polarization vector of the laser field is defined as $\hat{\mathbf{e}} = \hat{\mathbf{e}}_x \cos(\xi/2) + i\hat{\mathbf{e}}_y \sin(\xi/2)$, where ξ determines the polarization degree of the laser field, such as $\xi = \pi/2$ corresponds to circular polarization and $\xi = 0$ corresponds to linear polarization. The initial quantum state is expressed as $|\psi_i\rangle = \Phi_i(r) \otimes |l_1\rangle \otimes |l_2\rangle$, the eigenstate of the Hamiltonian $H_0 + U$ with the associated energy $E_i = -E_B + (l_1 + \frac{1}{2})\omega_1 + (l_2 + \frac{1}{2})\omega_2$, in which $\Phi_i(r)$ is the ground state wave function of the molecule with the binding energy E_B , $|l_1\rangle$ and $|l_2\rangle$ are the Fock states of the two laser modes. The final state of the system can be denoted by $|\psi_f\rangle = |\psi_{\mathbf{P}_f, m_1, m_2}\rangle$,

which is the quantized-field Volkov state in two-color laser fields that can be expressed as

$$\begin{aligned} \left| \psi_{\mathbf{p}_f m_1 m_2} \right\rangle = & V_e^{-1/2} \exp[i(\mathbf{P}_f + u_{p_1} \mathbf{k}_1 + u_{p_2} \mathbf{k}_2) \cdot \mathbf{r}] \times \sum_{\substack{q_1 = -m_1 \\ q_2 = -m_2}}^{\infty} \mathfrak{S}_{q_1, q_2}(\zeta)^* \\ & \times \exp\{-i[q_1(\mathbf{k}_1 \cdot \mathbf{r} + \phi_1) + q_2(\mathbf{k}_2 \cdot \mathbf{r} + \phi_2)]\} \left| m_1 + q_1, m_2 + q_2 \right\rangle \end{aligned} \quad (3)$$

where V_e is the normalized volume, \mathbf{p}_f is the final state momentum of the ionized electron, and $u_{p_1} = U_{p_1} / \omega_1$ ($u_{p_2} = U_{p_2} / \omega_2$), with U_{p_1} (U_{p_2}) being the ponderomotive potential in the laser field. \mathbf{k}_1 (\mathbf{k}_2) denotes photon momentum of the laser field. The total energy of final state is

$$E_{\mathbf{p}_f m_1 m_2} = \frac{\mathbf{P}_f^2}{2} + (m_1 + \frac{1}{2})\omega_1 + (m_2 + \frac{1}{2})\omega_2 + u_{p_1} \omega_1 + u_{p_2} \omega_2, \quad (4)$$

where m_1 (m_2) is the photon number in the laser field. The generalized Bessel function $\mathfrak{S}_{q_1, q_2}(\zeta)$ can be written as

$$\begin{aligned} \mathfrak{S}_{q_1, q_2}(\zeta) = & \sum_{q_3 q_4 q_5 q_6} J_{-q_1 + 2q_3 + q_5 + q_6}(\zeta_1) J_{-q_2 + 2q_4 + q_5 - q_6}(\zeta_2) \\ & J_{-q_3}(\zeta_3) J_{-q_4}(\zeta_4) J_{-q_5}(\zeta_5) J_{-q_6}(\zeta_6), \end{aligned} \quad (5)$$

with $\zeta \equiv (\zeta_1, \zeta_2, \zeta_3, \zeta_4, \zeta_5, \zeta_6)$,

$$\begin{aligned} \zeta_1 &= 2\sqrt{\frac{u_{p_1}}{\omega_1}} |\mathbf{p}_f \cdot \hat{\boldsymbol{\epsilon}}_1|, \quad \zeta_2 = 2\sqrt{\frac{u_{p_2}}{\omega_2}} |\mathbf{p}_f \cdot \hat{\boldsymbol{\epsilon}}_2|, \\ \zeta_3 &= \frac{1}{2} u_{p_1} \cos \xi_1, \quad \zeta_4 = \frac{1}{2} u_{p_2} \cos \xi_2, \\ \zeta_5 &= 2\sqrt{\frac{u_{p_1} u_{p_2} \omega_1 \omega_2}{\omega_1 + \omega_2}}, \quad \zeta_6 = 2\sqrt{\frac{u_{p_1} u_{p_2} \omega_1 \omega_2}{\omega_1 - \omega_2}}. \end{aligned} \quad (6)$$

Now, the transition matrix element of ATI process can be written as

$$T_d = \langle \psi_f | V | \psi_i \rangle = V_e^{-1/2} [(u_{p_1} - q_1)\omega_1 + (u_{p_2} - q_2)\omega_2] \mathfrak{S}_{q_1, q_2}(\zeta_f) \Phi_i(\mathbf{P}), \quad (7)$$

with $q_1 = l_1 - m_1$ ($q_2 = l_2 - m_2$) being the number of photons the electrons absorbing from two-color laser fields. And $\Phi_i(\mathbf{P})$ is the Fourier

transform of the initial wave function $\Phi_i(r)$.

III. NUMERICAL RESULTS

We may find from Eq. (7) that the transition matrix element is proportional to the wave function, *i.e.*, $T_d \propto \Phi_i(\mathbf{P})$, which indicates that the structure of the wave function can be mapped on the ATI spectrum. Therefore, the molecular structure information can be obtained by analyzing the ATI spectrum as these wave functions carrying the information, where the ATI spectrum satisfies some suitable conditions. In this section, we demonstrate that the two-color laser fields can provide such suitable ATI spectra to realize imaging molecules.

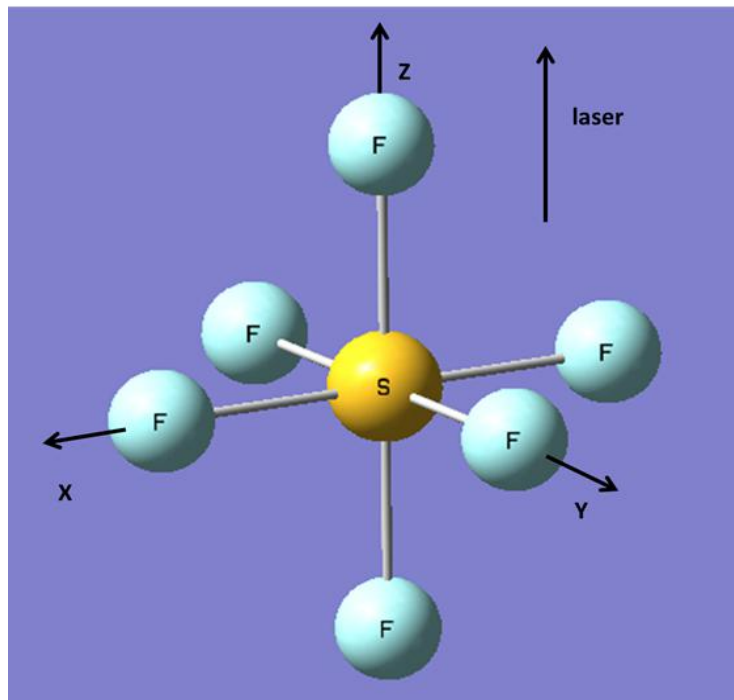


FIG 1. The skeleton of SF_6 molecules. The vector potentials of the two-color laser fields are along Z axis.

We now consider the ATI processes of molecule SF_6 in two-color laser fields. The ionization potential of SF_6 is 15.7eV [34]. Figure 1

shows the skeleton of the molecule SF₆, the origin of the coordinate system is set at the S atom. Atomic units are used throughout unless stated otherwise.

By using HF/6-311G* method [35-36] implemented by the Molpro software [37], the highest occupied molecular orbital (HOMO) of the SF₆ molecule includes three degenerated orbitals, which can be denoted as ψ_1 , ψ_2 and ψ_3 , according to their own symmetries. Here, the standard S-F bond length used in the calculation is $R_{SF}=2.929$ a.u..

According to the formula of Fourier transformation

$$\varphi(\mathbf{p}) = \frac{1}{(2\pi\hbar)^{3/2}} \int \psi(\mathbf{r}) e^{-i\mathbf{p}\cdot\mathbf{r}/\hbar} d^3r \quad , \quad (8)$$

we can obtain the wave functions for the three HOMO orbitals in momentum space. Firstly, we analyze the case of the SF₆ when the symmetry is ψ_1 . The expression of the HOMO wave function ψ_1 in momentum space is Eq. (A4) in the Appendix A, and its density distribution in coordinate space is shown in Fig. A1.

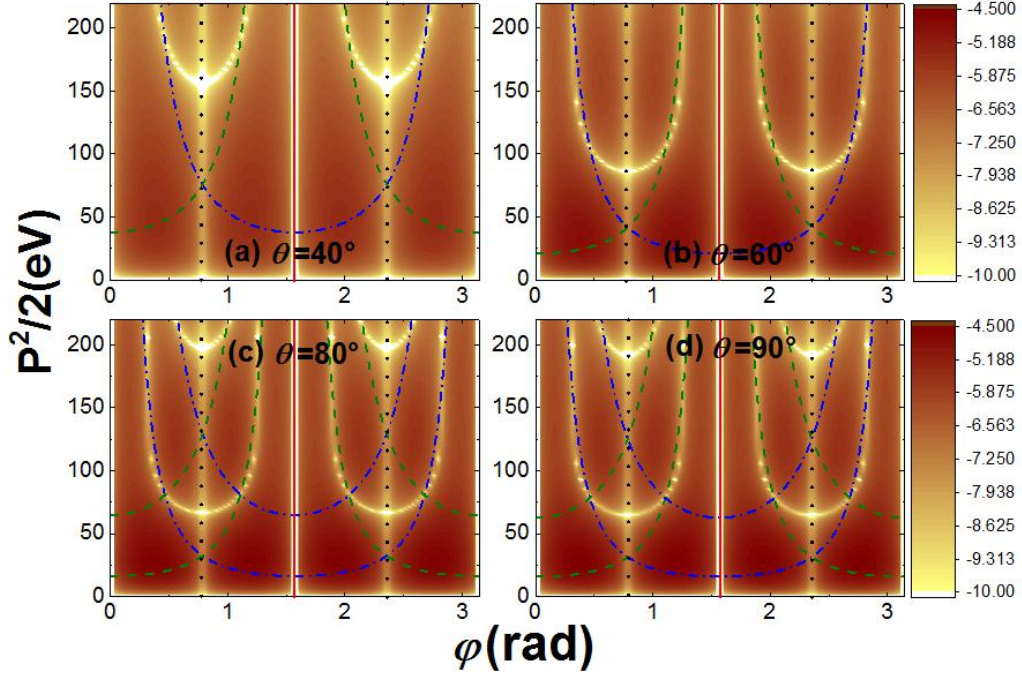


FIG. 2. The density distribution of ψ_1 wave function in momentum space for molecule SF_6 .

Figure 2 shows density distribution of the wave function ψ_1 of SF_6 in momentum space with different zenith angles, where the horizontal axis represents azimuthal angle and vertical axis represents $p^2/2$ dependent on momentum. One may clearly find that there are many fringes in the density distribution of the wave function as shown in Fig. 2. By analyzing Eq. (A4), we may find that these fringes can be classified by three types: (1) when $\varphi=n\pi/2$ with $n=1,2,\dots$, the amplitude of the wave function is zero because of the dependence of each term in Eq. (A4) on the momentum p_x and p_y , which is denoted by the red solid line in Fig. 2; (2) when $\varphi=n\pi/2+\pi/4$ with $n=0,1,\dots$, i.e., $p_x=\pm p_y$, the interference between each two corresponding terms in Eq. (A4) provides the destructive fringes in the density distribution of the wave function, as

shown by the black dotted lines in Fig. 2; (3) Besides above fringes, we may find there exist more fringes with the energy increasing, as shown in Fig. 2. In fact, when the value of the energy is large enough, where the exponent part in each term of Eq. (A4) affects dramatically its value, the wave function ψ_1 can be approximately expressed by two terms, i.e.,

$$\begin{aligned} \psi_1 \approx & -2.74966 \times 10^5 p_y \sin(R_{\text{SF}} p_x) e^{-\frac{p^2}{221.764}} \\ & + 2.74966 \times 10^5 p_x \sin(R_{\text{SF}} p_y) e^{-\frac{p^2}{221.764}}, \end{aligned} \quad (9)$$

hence, there will occur destructive fringes as one of the two terms becomes zero, which provide two fringes formula:

$$E = 0.5(n\pi)^2 / (\sin^2 \theta_f \cos^2 \varphi_f R^2), \quad (10)$$

and

$$E = 0.5(n\pi)^2 / (\sin^2 \theta_f \sin^2 \varphi_f R^2), \quad (11)$$

where R is the S-F bond length. The green dashed and blue dash-dot lines in Fig. 2 are predicted by Eq. (10) and (11), respectively. We should notice that these lines for third types of fringes agree well with that of numerical results as the energy is larger than 150 eV. However, these fringes are blurred in the low energy region. This is because that more terms in the wave function in Eq. (A4) play an important role in the distribution in low energy region and their contributions destroy these fringe structures.

From the above analysis, we may find that the third type of the interference fringes in the density distribution of the wave function

carries the information of the molecular structure, especially from the fringes of the distribution in high energy region. Therefore, according to the characteristic of the ATI spectrum predicted by Eq. (9), on which the density distribution of the molecular wave function maps, it is necessary to increase the energy of the ionized electron in order to increase the high energy part of the ATI spectrum. Here, we realize this idea by using IR+XUV two-color laser fields.

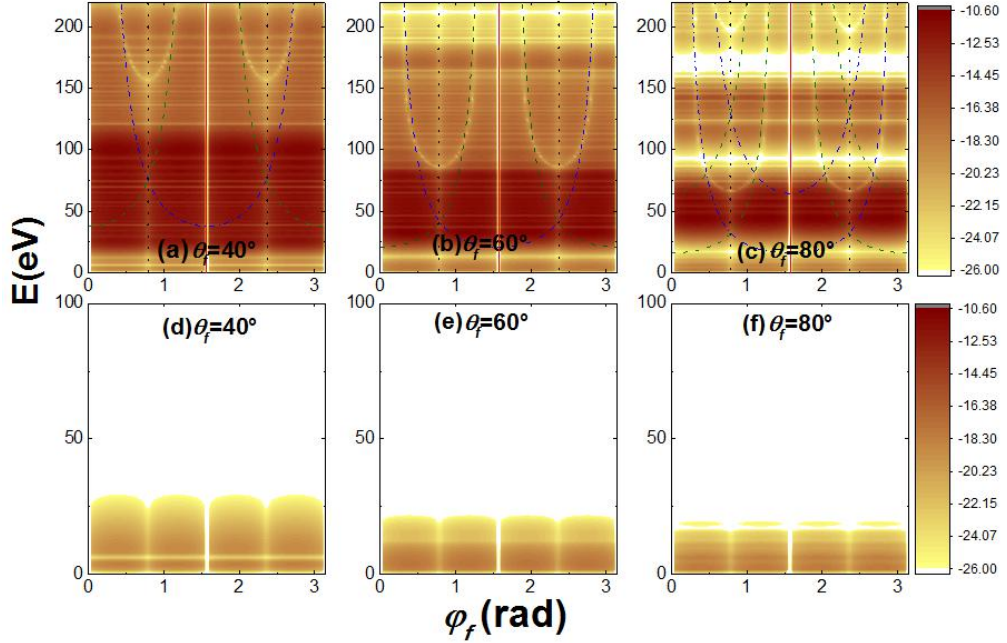


FIG. 3. The angle-resolved ATI spectra of SF_6 for initial state ψ_1 in the IR+XUV two-color fields (a-c) and monochromatic IR laser field (d-f) at $\theta_f = 40^\circ$ (a and d), 60° (b and e) and 80° (c and f).

According to the interference formulas of Eq. (10) and (11), we can find that the energy increases dramatically as the angle between the direction of the laser polarization and the electron momentum direction decreases towards zero, hence the angle is chosen as $\theta_f \in (20^\circ, 90^\circ)$. In this

paper, the polarization of the two-color linearly polarized laser field is along z axis, as shown in Fig. 1. The intensities of the two laser fields are $I_1=I_2=1.0\times 10^{14}$ W/cm², and the frequency $\omega_1=1.55$ eV and $\omega_2=50\omega_1$. The initial phases of the two-color laser fields are $\phi_1=\phi_2=0^\circ$ for simplicity. Figure 3 (a-c) shows the ATI spectra in IR+XUV two color laser fields for initial wave function ψ_1 of SF₆ with the angle between the momentum direction of the electron and the polarization direction of the IR laser $\theta_f = 40^\circ$ (a), 60° (b) and 80° (c). For comparison, we also present the ATI spectrum by IR laser field in Fig. 3 (d-f) with the laser frequency $\omega=1.55$ eV and intensity $I=1.0\times 10^{14}$ W/cm² for $\theta_f = 40^\circ$ (d), 60° (e) and 80° (f). One may find that, the energy region of the ATI spectra for the monochromatic IR laser case is below 50eV, while the energy region of the ATI spectrum is enlarged obviously by using the IR+XUV laser fields as shown in Fig. 3. This result is attributed to that the participation of XUV laser improves the ionization probability, and the IR laser field accelerates the photoelectron during the ATI process [32]. In addition, the ATI spectra present multi-plateau structure, where the width of each plateau in the ATI spectrum decreases as the angle θ_f increases. These spectrum structures are determined by the energy conservation during the ionization process [33], where the cutoff of each plateau decreases with the angle increasing. More interestingly, we may find that the interference fringes emerge in the high energy region of these spectra, which are

attributed to the interference fringes in the density distribution of the molecular wave function shown in Fig. 2. The green dashed and blue dash-dot lines are also from the interference formula of Eqs. (10) and (11), where the high energy part of these lines agrees well with the numerical results shown in Fig. 3. This result indicates that the analysis of the wave function which can be simplified by two terms in high energy region is suitable.

From Eqs. (10) and (11), we can derive the formulas about molecular bond length, which is

$$R = n\pi / (\sqrt{2E} |\sin \theta_f| |\cos \varphi_f|), \quad (12)$$

$$R = n\pi / (\sqrt{2E} |\sin \theta_f| |\sin \varphi_f|). \quad (13)$$

Therefore, by using the data of the ATI spectra, we can predict the S-F bond length of SF₆ by Eqs. (12) and (13), which are shown in Tables 1 and 2. The error in both tables is defined as $\Delta = (R_{avg} - R_{SF}) / R_{SF}$. We can find that the error is smaller than 8% in both cases.

Tab. 1. The length of S-F bond length in SF₆ molecule by Eq. (12), where the data are taken from the ATI spectra shown in Fig. 3 for the molecular wave function of ψ_1 .

θ_f	φ_f / rad	E/eV	R/a.u.	$R_{avg}/\text{a.u.}$	Error Δ
40°	1.12	190	3.00	3.03	3.45%
	2.02	190	3.01		
	1.15	210	3.04		
	1.99	210	3.06		
60°	1.26	190	3.17	3.10	5.84%
	1.88	190	3.19		
	1.26	210	3.02		

	1.88	210	3.03		
80°	1.26	190	2.79	2.73	6.79%
	1.88	190	2.80		
	1.26	210	2.65		
	1.88	210	2.67		

Tab. 2. The length of S-F bond length in SF₆ molecule by Eq. (13), where the data are taken from the ATI spectra shown in Fig. 3 for the molecular wave function of ψ_1 .

θ_f	φ_f/rad	E /eV	R/a.u.	$R_{\text{avg}}/\text{a.u.}$	Error Δ
40°	0.45	190	3.01	3.03	3.45%
	2.69	190	3.00		
	0.42	210	3.05		
	2.72	210	3.04		
60°	0.31	190	3.18	3.10	5.84%
	2.83	190	3.17		
	0.31	210	3.03		
	2.83	210	3.01		
80°	0.31	190	2.80	2.72	7.14%
	2.83	190	2.78		
	0.31	210	2.66		
	2.83	210	2.65		

From the above discussion we can see that the wave function of ψ_1 in momentum space can be simplified by two main effective terms in Eq. (9). We now trace back to the coordinate space wave function, which corresponds to four main effective terms expressed as

$$\begin{aligned} \psi'_1 = \frac{1}{\sqrt{2}} \{ & 1.78005y \exp\{-55.4441[(x-2.929)^2 + y^2 + z^2]\} \\ & -1.78005y \exp\{-55.4441[(x+2.929)^2 + y^2 + z^2]\} \\ & -1.78005x \exp\{-55.4441[x^2 + (y-2.929)^2 + z^2]\} \\ & +1.78005x \exp\{-55.4441[x^2 + (y+2.929)^2 + z^2]\} \} \end{aligned} \quad (14)$$

We find that these four terms are from four F atoms in XY plane perpendicular to the direction of the laser field as shown in Fig.4.

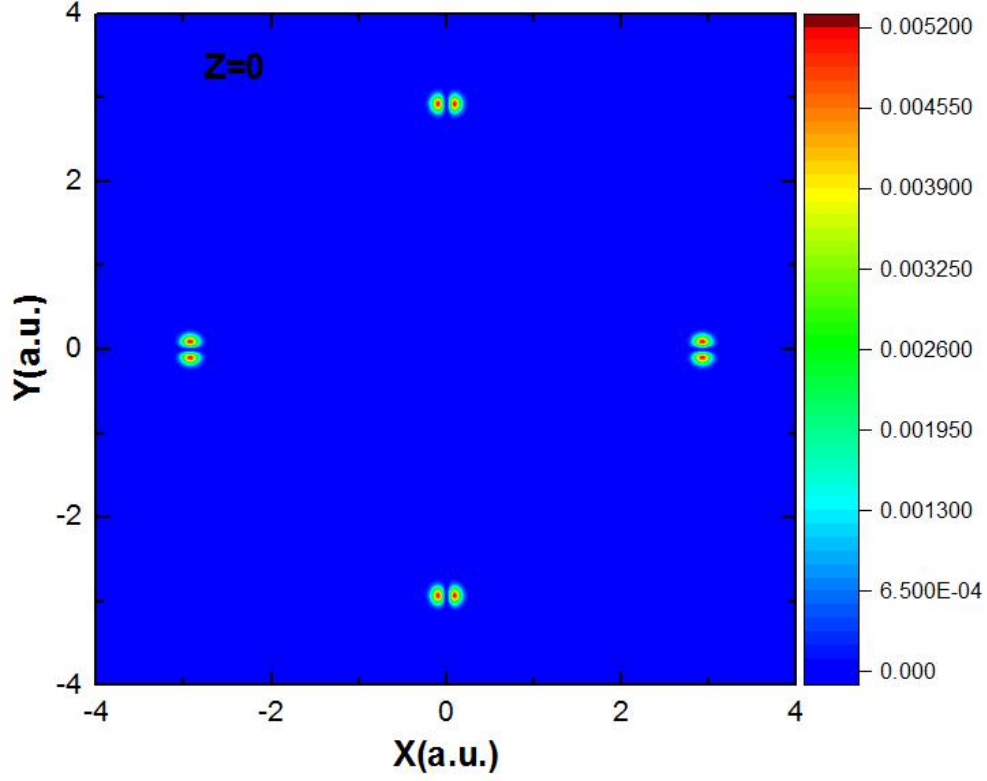


FIG. 4. The density distribution of the wave function by Eq. (14) in XY plane in coordinate space with the value of $Z=0$ a.u..

We now consider imaging the wave function of ψ_2 and ψ_3 by ATI spectra. Since the polarization direction of the two-color laser fields is along Z axis, the ATI spectra for both wave functions ψ_2 and ψ_3 are similar, hence we only present the results for wave function ψ_2 .

The wave function of ψ_2 in momentum space is presented in Eq. (A5) of Appendix A, where the density distribution of this wave function is shown in Fig. 5.

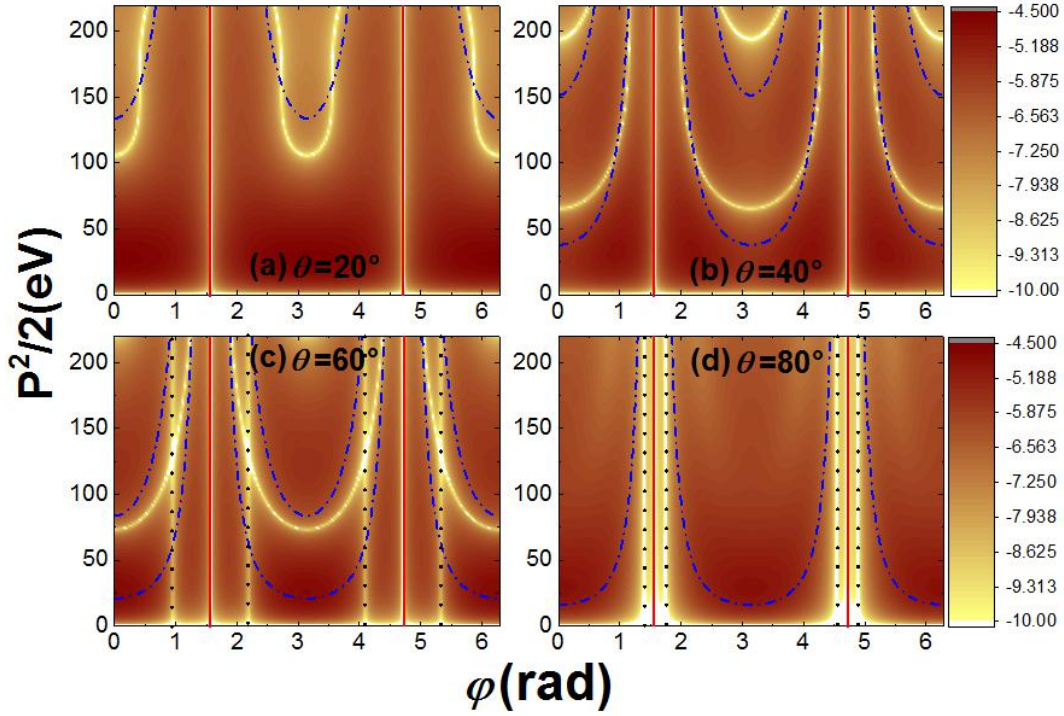


FIG. 5. The density distribution of ψ_2 wave function in momentum space for molecule SF_6 .

Similarly for the case of ψ_1 , there also exists three types of fringes: (1) when $\varphi = \pi/2 + n\pi$ with $n=1,2,\dots$, the amplitude of the wave function is zero because each term in Eq. (A5) depends on the momentum p_x , which is denoted by the red solid line in Fig. 5; (2) when $\cos\varphi = \pm \text{ctg}\theta$, i.e., $p_x = \pm p_z$, the interference between each two corresponding terms in Eq. (A5) provides the destructive fringes in the density distribution of the wave function, as shown by the black dotted lines in Figs. 5(c) and (d); (3) besides above fringes, we may also find some special fringes which carry the information of the molecular structure in the high energy region where these fringes can be predicted by the blue dash-dot lines in Fig. 5. These dash-dot lines can be obtained by simplifying the wave function of ψ_2 in Eq. (A5) with two terms for the momentum being large enough:

$$\begin{aligned} \psi_2 \approx & -2.74966 \times 10^5 p_z \sin(R_{\text{SF}} p_x) e^{-\frac{p^2}{221.764}} \\ & + 2.74966 \times 10^5 p_x \sin(R_{\text{SF}} p_z) e^{-\frac{p^2}{221.764}} . \end{aligned} \quad (15)$$

Therefore, we may obtain an interference formula by the first term of above equation, which can be written as

$$E = 0.5(n\pi)^2 / (\sin^2 \theta_f \cos^2 \varphi_f R^2). \quad (16)$$

The blue dash-dot lines in Fig. 5 are drawn by Eq. (16). It can be found that these dash-dot lines agree with the fringes in high energy region, with E larger than about 150eV, in the density distribution of the wave function.

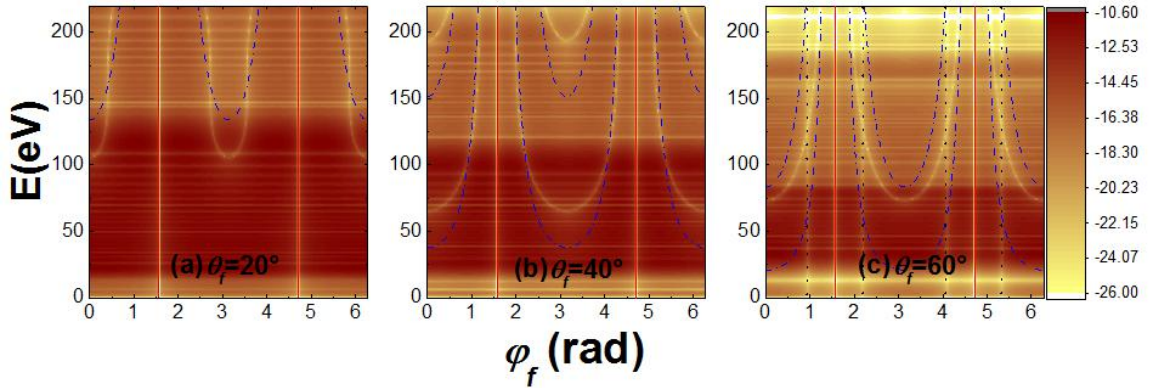


FIG. 6. The total angle-resolved ATI spectra of SF₆ for initial state ψ_2 .

Figure 6 shows the angle-resolved ATI spectra of SF₆ for the initial state of ψ_2 with the angle $\theta_f = 20^\circ$ (a), 40° (b) and 60° (c). The blue dash-dot lines in Fig. 6 are predicted by Eq. (16). By using these fringes, we can also derive the S-F bond length by the following formula, which is obtained from Eq. (16):

$$R = n\pi / (\sqrt{2E} |\sin \theta_f| |\cos \varphi_f|). \quad (17)$$

Table 3 presents the predictions of the S-F bond length by using the data

of the numerical calculation shown in Fig. 6. We can find that the error shown in Table 3 is smaller than 10%.

Tab. 3. The calculation results of the S-F bond length of SF₆ when the symmetry is ψ_2 by Eq. (17).

θ_f	φ_f /rad	E /eV	R/a.u.	R_{avg} /a.u	Error Δ
20°	0.42	190	2.69	2.69	8.16%
	2.72	190	2.69		
	3.56	190	2.69		
	5.87	190	2.68		
40°	1.15	190	3.20	3.21	9.59%
	1.99	190	3.21		
	4.29	190	3.19		
	5.13	190	3.22		
60°	1.19	190	2.70	2.68	8.50%
	1.95	190	2.71		
	4.32	190	2.63		
	5.10	190	2.66		

Similarly, the wave function of Eq. (15) in momentum space corresponds to four effective terms of the wave function written as Eq. (18) in the coordinate space

$$\begin{aligned}
\psi'_2 = \frac{1}{\sqrt{2}} \{ & 1.78005z \exp\{-55.444[(x-2.929)^2 + y^2 + z^2]\} \\
& -1.78005z \exp\{-55.444[(x+2.929)^2 + y^2 + z^2]\}, \\
& -1.78005x \exp\{-55.444[x^2 + y^2 + (z-2.929)^2]\} \\
& +1.78005x \exp\{-55.444[x^2 + y^2 + (z+2.929)^2]\}
\end{aligned} \tag{18}$$

which is pertinent to four F atoms in XZ plane, as shows in Fig. 7.

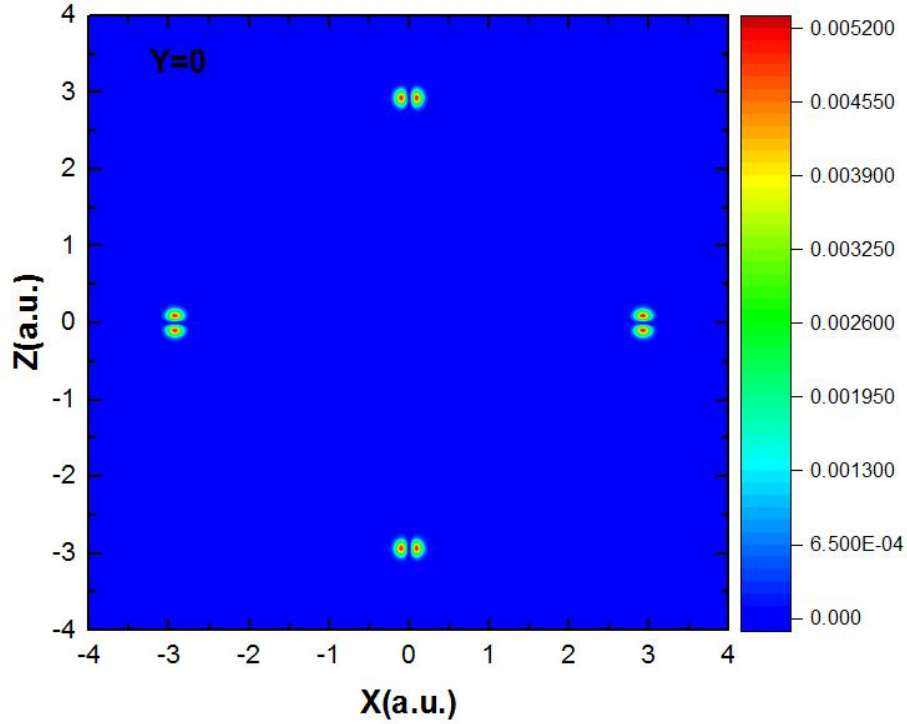


Fig. 7. The density distribution of the wave function Eq. (18) in XZ plane in coordinate space for $Y=0$ a.u..

Now we consider the ATI spectrum of the HOMO-1 orbitals, where there exist three HOMO-1 degenerate orbitals denoted by ψ_4 , ψ_5 , and ψ_6 . Fig. 8. shows the angle-resolved ATI spectra for the HOMO-1 wave function ψ_4 , where we may find that the probability of this spectrum is much smaller than that of the corresponding ATI spectrum for the HOMO wave functions. The other two wave functions, i.e., ψ_5 and ψ_6 , present similar results. One reason for these results is that the ionization threshold of HOMO-1 orbitals, which is 14.6eV, is much smaller than XUV photon energy 77.5eV, thereby, although the detuning for HOMO-1 orbitals is a little larger than that for HOMO orbitals, this difference is so small that it can be ignored. The other crucially important reason is that the momentum space wave function of HOMO-1 orbitals is more diffuse,

which can be found in Eq. (B1) in the appendix B, thereby the ionization probability of the HOMO-1 orbits is much lower than that of the HOMO orbits for the photoelectron energy in the region of 0 to 220 eV. As a result, the contribution of the HOMO-1 wave functions to the ATI spectrum can be ignored under our present laser conditions.

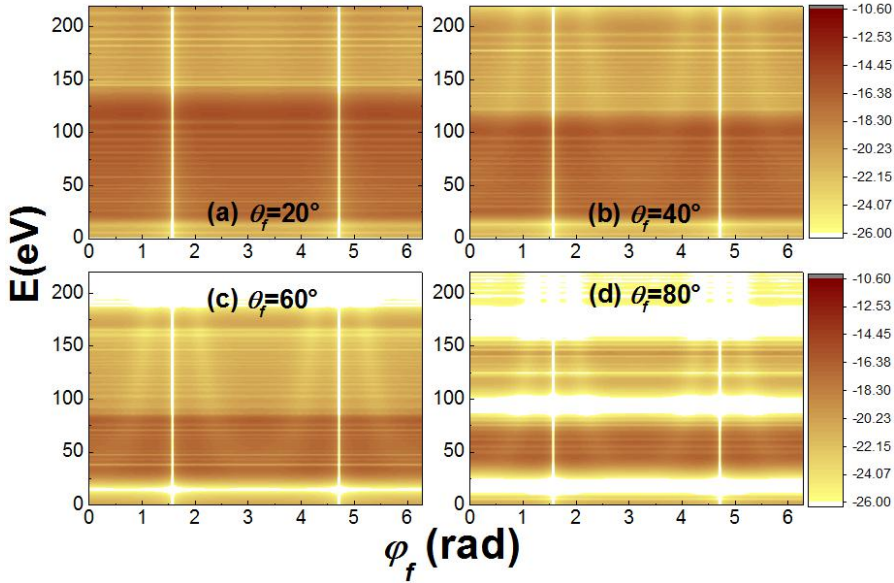


FIG. 8. The total angle-resolved ATI spectra of SF_6 for the HOMO-1 wave function ψ_4 .

IV. CONCLUSIONS

In summary, we have imaged the structures of complex symmetric polyatomic molecules SF_6 by using IR+XUV two-color laser fields. We find that the complex wave function of the molecule can be simplified by few terms in high energy region, hence some destructive interference formula carrying molecular information can be obtained by analyzing these terms. Furthermore, since the angle-resolved ATI spectrum is

proportional to the molecular wave function, the destructive interference fringes in the ATI spectra in high energy region can be used to derive the molecular information according to the interference formulas which is from the simplified molecular wave function. For SF₆ molecule, because it has a high degree of symmetry, the destructive interference fringes in high energy part of ATI spectrum can provide effective information to predict the bond length of S-F for the three HOMO wave functions. In this work, we put forward a novel path of utilizing two color laser fields to extract the molecular structure information from frequency domain perspective, which is effective for imaging complex polyatomic molecules.

ACKNOWLEDGEMENTS

This work was supported by the National Natural Science Foundation of China under Grant Nos. 11774411, 11474348, 11674198 and 11425414. And we thank all the members of strong-field atomic and molecular physics (SFAMP) club for their helpful discussions and suggestions.

- [1] P. Agostini, F. Fabre, G. Mainfray, G. Petite, N. K. Rahman, Free-free transitions following six-photon ionization of xenon atoms, *Phys. Rev. Lett.* **42** 1127 (1979).
- [2] G. G. Paulus, W. Nicklich, H. L. Xu, P. Lambropoulos, H. Walther, Plateau in above threshold ionization spectra, *Phys. Rev. Lett.* **72**, 2851(1994).
- [3] W. Becker, F. Grasbon, R. Kopold, D. B. Milosevic, G. G. Paulus, H. Walther, Above-threshold ionization: from classical features to quantum effects, *Adv. Atom. Mol. Opt. Phy.* **48**, 35 (2002).

- [4] S. Odzak, A. Cerbic, M. Busuladzic, E. Hasovic, A. Gazibegovic, D. B. Milosevic, Heteronuclear diatomic molecules in a strong laser field with an arbitrary polarization, *Phys. Scr.* **T162**, 014012(2014).
- [5] I. Petersen, J. Henkel, M. Lein, Signatures of molecular orbital structure in lateral electron momentum distributions from strong-field ionization, *Phys. Rev. Lett.* **114**, 103004(2015).
- [6] K. Yuan, A. D. Bandrauk, Molecular above-threshold-ionization angular distributions with intense circularly polarized attosecond XUV laser pulses, *Phys. Rev. A* **85**, 053419(2012).
- [7] M. R. He, Y. Li, Y. M. Zhou, M. Li, W. Cao, and P. X. Lu, Direct visualization of valence electron motion using strong-field photoelectron holography, *Phys. Rev. Lett.* **120**, 133204 (2018).
- [8] P. B. Corkum, Plasma perspective on strong-field multiphoton ionization, *Phys. Rev. Lett.* **71**, 1994(1993)
- [9] G. G. Paulus, W. Becker, W. Nicklich, H. Walther, Rescattering effects in above-threshold ionization: a classical model, *J. Phys. B.* **27**, L703 (1994).
- [10] G. G. Paulus, W. Becker, H. Walther, Classical rescattering effects in two-color above-threshold ionization, *Phys. Rev. A.* **52**, 4043 (1995).
- [11] D. B. Milosevic, G. G. Paulus, D. Bauer, W. Becker, Above-threshold ionization by few-cycle pulses, *J. Phys. B.* **39**, R203(2006).
- [12] A. L'Huillier, K. Schafer, and K. Kulander, High-order harmonic generation in xenon at 1064nm: the role of phase matching, *Phys. Rev. Lett.* **66**, 2200 (1991).
- [13] M. Lewenstein, P. Balcou, M. Ivanov, A. L'Huillier, and P. B. Corkum, Theory of high-harmonic generation by low-frequency laser fields, *Phys. Rev. A* **49**, 2117 (1994).
- [14] M. Busuladzic, A. Gazibegovic, D. B. Milosevic, W. Becker, Angle-resolved high-order above-threshold ionization of a molecule: sensitive tool for molecular characterization, *Phys. Rev. Lett.* **100**, 203003(2008).
- [15] Y. Guo, P. Fu, Z.-C. Yan, J. Gong, B. Wang, Imaging the geometrical structure of the H_2^+ molecular ion by high-order above-threshold ionization in an intense laser field, *Phys. Rev. A* **80**, 063408 (2009).
- [16] H. Kang, W. Quan, Y. Wang, Z. Lin, M. Wu, H. Liu, X. Liu, B. Wang, H. Liu, Y. Gu, X. Jia, J. Liu, J. Chen, Y. Cheng, Structure effects in angle-resolved high-order above-threshold ionization of molecules, *Phys. Rev. Lett.* **104**, 203001 (2010).
- [17] R. Sun, X. Lai, S. Yu, Y. Wang, S. Xu, W. Quan, and X. Liu, Tomographic extraction of the internuclear separation based on two-center interference with aligned diatomic molecules, *Phys. Rev. Lett.* **122**, 193202 (2019).
- [18] Y. He, L. He, P. Lan, B. Wang, L. Li, X. Zhu, W. Cao, and P. Lu, Direct imaging

- of molecular rotation with high-order-harmonic generation, *Phys. Rev. A* **99**, 053419 (2019).
- [19] B. Zhang, M. Lein, High-order harmonic generation from diatomic molecules in an orthogonally polarized two-color laser field, *Phys. Rev. A* **100**, 043401 (2019).
- [20] B. Wang, Y. Guo, B. Zhang, Z. Zhao, Z.-C. Yan and P. Fu, Charge-distribution effect of imaging molecular structure by high-order above-threshold ionization, *Phys. Rev. A* **82**, 043402 (2010).
- [21] M. Kübel, Z. Dube, A.Yu. Naumov, D. M. Villeneuve, P. B. Corkum and A. Staudte, Spatiotemporal imaging of valence electron motion, *Nat. Comm.* **10**, 1042(2019).
- [22] F. Kelkensberg, C. Lefebvre, W. Siu, O. Ghafur, T. T. Nguyen-Dang, O. Atabek, A. Keller, V. Serov, P. Johnsson, M. Swoboda, T. Remetter, A. L’Huillier, S. Zherebtsov, G. Sansone, E. Benedetti, F. Ferrari, M. Nisoli, F. Le’pine, M. F. Kling, and M. J. J. Vrakking, Molecular dissociative ionization and wave-packet dynamics studied using two-color XUV and IR pump-probe spectroscopy, *Phys. Rev. Lett.* **103**, 123005(2009)
- [23] M. J. J. Vrakking, Attosecond imaging, *Phys.Chem.Chem.Phys.* **16**, 2775(2014).
- [24] G. Schmid, K.Schnorr, S. Augustin, S. Meister, H. Lindenblatt, F. Trostl, Y. F. Liu, T. Miteva, M. Gisselbrecht, S. Düsterer, H. Redlin, R. Treusch, K. Gokhberg, A. I. Kuleff, L. S. Cederbaum, C. D. Schröter, T. Pfeifer, and R. Moshhammer, Tracing charge transfer in argon dimers by XUV-pump IR-probe experiments at FLASH, *J. Chem. Phys.* **151**, 084314 (2019).
- [25] W. Hu, Y. Liu, S. Luo, X. Li, J. Yu, X. Li, Z. Sun, K. Yuan, A. D. Bandrauk, and D. Ding, Coherent interference of molecular electronic states in NO by two-color femtosecond laser pulses, *Phys. Rev. A* **99**, 011402(R) (2019).
- [26] T. Endo, H. Fujise, H. Hasegawa, A. Matsuda, M. Fushitani, O. I. Tolstikhin, T.Morishita, and A. Hishikawa, Angle dependence of dissociative tunneling ionization of NO in asymmetric two-color intense laser fields, *Phys. Rev. A* **100**, 053422 (2019)
- [27] Z. Chen, and F. He, Alignment-dependent ionization of nonlinear triatomic molecules in strong laser fields, *J. Opt. Soc. Am. B* **36**,2571 (2019).
- [28] M. Okunishi, Y. Ito, V. Sharma, S. Aktar, K. Ueda, R. R. Lucchese, A. I. Dnestryan, O. I. Tolstikhin, S. Inoue, H. Matsui, and T. Morishita, Rescattering photoelectron spectroscopy of the CO₂ molecule: progress towards experimental discrimination between theoretical target-structure models, *Phys. Rev. A* **100**, 053404 (2019).
- [29] D.-S. Guo and T. Åberg, Quantum electrodynamical approach to multiphoton ionisation in the high-intensity H field, *J. Phys. A: Math. Gen.* **21**, 4577 (1988); D.-S. Guo and G. W. F. Drake, Stationary solutions for an electron in an intense laser field. I. Single-mode case, *ibid.* **25**, 3383 (1992).
- [30] B. Wang, L. Gao, X. Li, D.-S. Guo and P. Fu, Frequency-domain theory of high-order above-threshold ionization based on nonperturbative quantum electrodynamics, *Phys. Rev. A* **75**, 063419 (2007).

- [31] B. Wang, Y. Guo, J. Chen, Z.-C. Yan and P. Fu, Frequency-domain theory of nonsequential double ionization in intense laser fields based on nonperturbative QED, *Phys. Rev. A* **85**, 023402 (2012).
- [32] F. Jin, Y. Tian, J. Chen, Y. Yang, X. Liu, Z.-C. Yan, and B. Wang, Nonsequential double ionization of helium in IR+XUV two-color laser fields: collision-ionization process, *Phys. Rev. A* **93**, 043417 (2016).
- [33] S. Shi, F. Jin and B. Wang, Angle-resolved spectra of the direct above-threshold ionization of diatomic molecule in IR+XUV laser fields, *Chin. Phys. B* **28**, 023202 (2019)
- [34] N.-T. Nguyen, R. R. Lucchese, C. D. Lin, A.-T. Le, Probing and extracting the structure of vibrating SF₆ molecules with inner-shell photoelectrons, *Phys. Rev. A* **93**, 063419 (2016).
- [35] H. J. Werner, P. J. Knowles, R. Lindh, F. R. Manby, M. Schutz, P. Celani, T. Korona, G. Rauhut, R. D. Amos, A. Bernhardsson, A. Berning, D. L. Cooper, M. J. O. Deegan, A. J. Dobbyn, F. Eckert, C. Hampel, G. Hetzer, A. W. Lloyd, S. J. McNicholas, W. Meyer, M. E. Mura, A. Nicklass, P. Palmieri, et al. Molpro, APackage of ab initio Programs (Version 2006.1) <http://www.molpro.net> [2018-12-12]
- [36] M. Schutz, R. Lindh, and H. Werner, Integral-direct electron correlation methods, *Mol. Phys.* **96** 719 (1999).
- [37] R. Krishnan, J. S. Binkley, R. Seeger, J. A. Pople, Selfconsistent molecular orbital methods. XX. A basis set for correlated wave functions, *J. Chem. Phys.* **72**, 650 (1980).

Appendix A

SF₆

The molecular orbitals are from LCAO (linear combination of atomic orbitals), and atomic orbitals consist of Gaussian functions, and we can obtain three molecular orbitals in coordinate space in the following part. Firstly, the orbital of ψ'_1 can be written as,

$$\begin{aligned} \psi'_1 = \frac{1}{\sqrt{2}} \{ & 1.78005y \exp\{-55.4441[(x-2.929)^2 + y^2 + z^2]\} + 1.87624y \exp\{-12.6323[(x-2.929)^2 + y^2 + z^2]\} \\ & + 1.40521y \exp\{-3.71756[(x-2.929)^2 + y^2 + z^2]\} - 1.78005y \exp\{-55.4441[(x+2.929)^2 + y^2 + z^2]\} \\ & - 1.87624y \exp\{-12.6323[(x+2.929)^2 + y^2 + z^2]\} - 1.40521y \exp\{-3.71756[(x+2.929)^2 + y^2 + z^2]\} \\ & + 0.614912y \exp\{-1.16545[(x-2.929)^2 + y^2 + z^2]\} - 0.614912y \exp\{-1.16545[(x+2.929)^2 + y^2 + z^2]\} \\ & + 0.111126y \exp\{-0.321892[(x-2.929)^2 + y^2 + z^2]\} - 0.111126y \exp\{-0.321892[(x+2.929)^2 + y^2 + z^2]\} \\ & - 0.0863376(x-2.929)y \exp\{-1.75[(x-2.929)^2 + y^2 + z^2]\} - 0.0863376(x+2.929)y \exp\{-1.75[(x+2.929)^2 + y^2 + z^2]\} \\ & - 1.78005x \exp\{-55.4441[x^2 + (y-2.929)^2 + z^2]\} - 1.87624x \exp\{-12.6323[x^2 + (y-2.929)^2 + z^2]\} \\ & - 1.40521x \exp\{-3.71756[x^2 + (y-2.929)^2 + z^2]\} + 1.78005x \exp\{-55.4441[x^2 + (y+2.929)^2 + z^2]\} \\ & + 1.87624x \exp\{-12.6323[x^2 + (y+2.929)^2 + z^2]\} + 1.40521x \exp\{-3.71756[x^2 + (y+2.929)^2 + z^2]\} \\ & - 0.614912x \exp\{-1.16545[x^2 + (y-2.929)^2 + z^2]\} + 0.614912x \exp\{-1.16545[x^2 + (y-2.929)^2 + z^2]\} \\ & - 0.111126x \exp\{-0.321892[x^2 + (y-2.929)^2 + z^2]\} + 0.111126x \exp\{-0.321892[x^2 + (y-2.929)^2 + z^2]\} \\ & + 0.0863376x(y-2.929) \exp\{-1.75[x^2 + (y-2.929)^2 + z^2]\} + 0.0863376x(y+2.929) \exp\{-1.75[x^2 + (y+2.929)^2 + z^2]\} \} \end{aligned} \quad , (A1)$$

which can be depicted in Fig. A1.

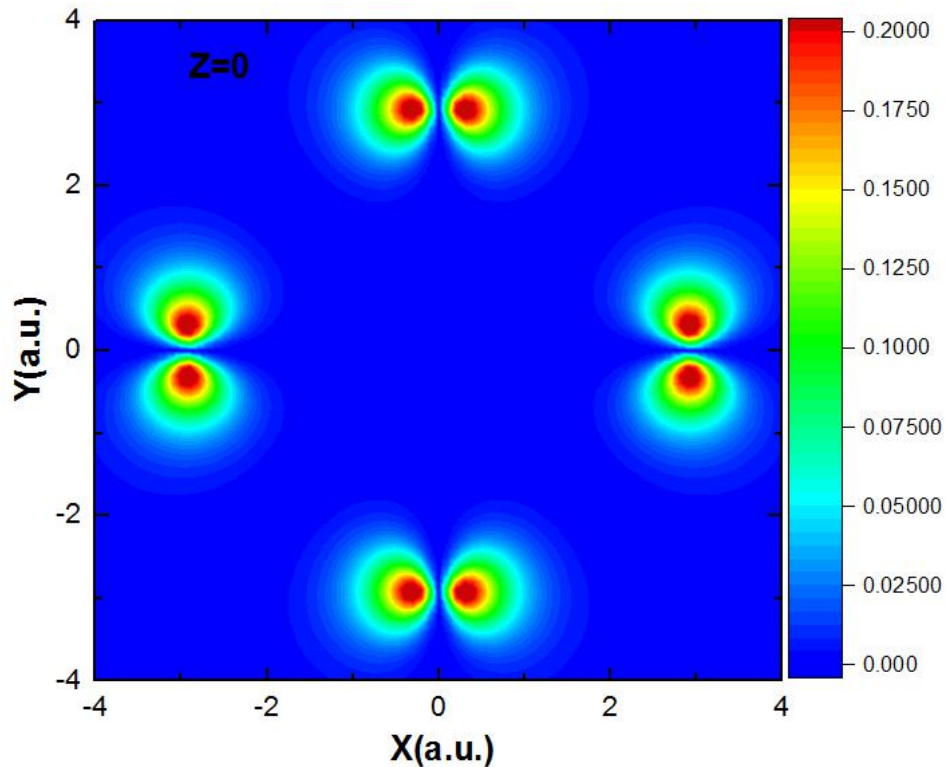


FIG. A1. The density distribution of wave function ψ'_1 in coordinate space with the value of $Z=0$ a.u..

The wave function for the symmetry of ψ'_2 is

$$\begin{aligned}
\psi'_2 = \frac{1}{\sqrt{2}} \{ & 1.78005z \exp\{-55.444[(x-2.929)^2 + y^2 + z^2]\} + 1.87624z \exp\{-12.6323[(x-2.929)^2 + y^2 + z^2]\} \\
& + 1.40521z \exp\{-3.71756[(x-2.929)^2 + y^2 + z^2]\} - 1.78005z \exp\{-55.444[(x+2.929)^2 + y^2 + z^2]\} \\
& - 1.87624z \exp\{-12.6323[(x+2.929)^2 + y^2 + z^2]\} - 1.40521z \exp\{-3.71756[(x+2.929)^2 + y^2 + z^2]\} \\
& + 0.614912z \exp\{-1.16545[(x-2.929)^2 + y^2 + z^2]\} - 0.614912z \exp\{-1.16545[(x+2.929)^2 + y^2 + z^2]\} \\
& + 0.111126z \exp\{-0.321892[(x-2.929)^2 + y^2 + z^2]\} - 0.111126z \exp\{-0.321892[(x+2.929)^2 + y^2 + z^2]\} \\
& - 0.0863376(x-2.929)z \exp\{-1.75[(x-2.929)^2 + y^2 + z^2]\} - 0.0863376(x+2.929)z \exp\{-1.75[(x+2.929)^2 + y^2 + z^2]\} \\
& - 1.78005x \exp\{-55.444[x^2 + y^2 + (z-2.929)^2]\} - 1.87624x \exp\{-12.6323[x^2 + y^2 + (z-2.929)^2]\} \\
& - 1.40521x \exp\{-3.71756[x^2 + y^2 + (z-2.929)^2]\} + 1.78005x \exp\{-55.444[x^2 + y^2 + (z+2.929)^2]\} \\
& + 1.87624x \exp\{-12.6323[x^2 + y^2 + (z+2.929)^2]\} + 1.40521x \exp\{-3.71756[x^2 + y^2 + (z+2.929)^2]\} \\
& - 0.614912x \exp\{-1.16545[x^2 + y^2 + (z-2.929)^2]\} + 0.614912x \exp\{-1.16545[x^2 + y^2 + (z+2.929)^2]\} \\
& - 0.111126x \exp\{-0.321892[x^2 + y^2 + (z-2.929)^2]\} + 0.111126x \exp\{-0.321892[x^2 + y^2 + (z+2.929)^2]\} \\
& + 0.0863376x(z-2.929) \exp\{-1.75[x^2 + y^2 + (z-2.929)^2]\} + 0.0863376x(z+2.929) \exp\{-1.75[x^2 + y^2 + (z+2.929)^2]\} \}
\end{aligned} \tag{A2}$$

which is shown by Fig. A2.

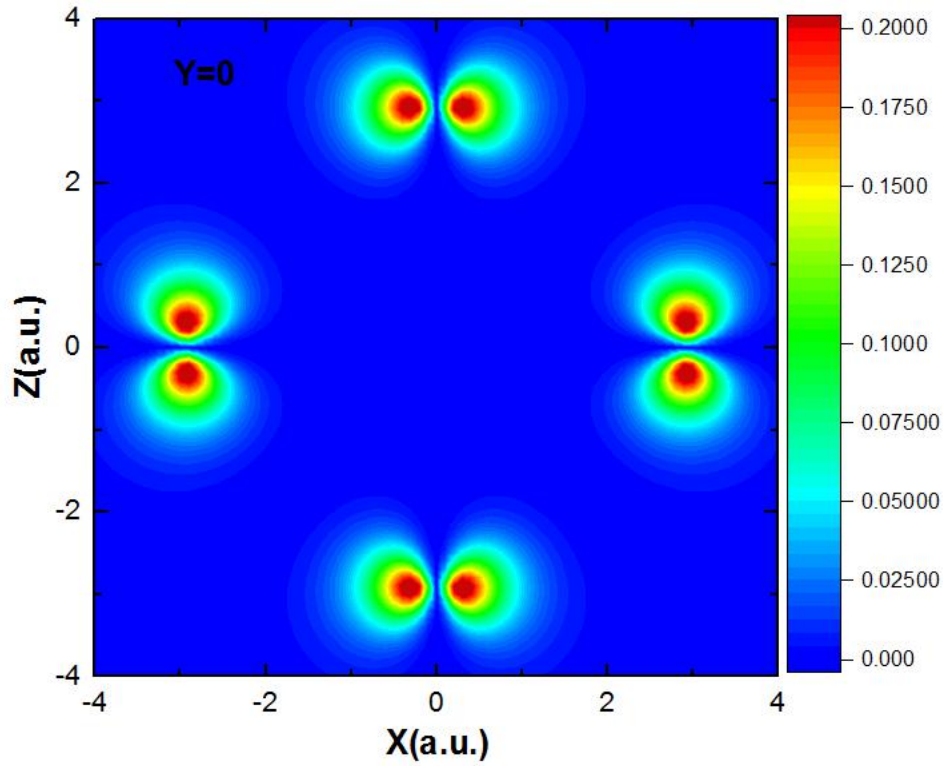


FIG. A2. The density distribution of wave function ψ'_2 in coordinate space with the value of $Y=0$ a.u..

The coordinate space wave function of ψ'_3 is

$$\begin{aligned}
\psi'_3 = & \frac{1}{\sqrt{2}} \{ 1.78005z \exp\{-55.444[x^2 + (y-2.929)^2 + z^2]\} + 1.87624z \exp\{-12.6323[x^2 + (y-2.929)^2 + z^2]\} \\
& + 1.40521z \exp\{-3.71756[x^2 + (y-2.929)^2 + z^2]\} - 1.78005z \exp\{-55.444[x^2 + (y+2.929)^2 + z^2]\} \\
& - 1.87624z \exp\{-12.6323[x^2 + (y+2.929)^2 + z^2]\} - 1.40521z \exp\{-3.71756[x^2 + (y+2.929)^2 + z^2]\} \\
& + 0.614912z \exp\{-1.16545[x^2 + (y-2.929)^2 + z^2]\} - 0.614912z \exp\{-1.16545[x^2 + (y+2.929)^2 + z^2]\} \\
& + 0.111126z \exp\{-0.321892[x^2 + (y-2.929)^2 + z^2]\} - 0.111126z \exp\{-0.321892[x^2 + (y+2.929)^2 + z^2]\} \\
& - 0.0863376(y-2.929)z \exp\{-1.75[x^2 + (y-2.929)^2 + z^2]\} - 0.0863376(y+2.929)z \exp\{-1.75[x^2 + (y+2.929)^2 + z^2]\} \\
& - 1.78005y \exp\{-55.444[x^2 + y^2 + (z-2.929)^2]\} - 1.87624y \exp\{-12.6323[x^2 + y^2 + (z-2.929)^2]\} \\
& - 1.40521y \exp\{-3.71756[x^2 + y^2 + (z-2.929)^2]\} + 1.78005y \exp\{-55.444[x^2 + y^2 + (z+2.929)^2]\} \\
& + 1.87624y \exp\{-12.6323[x^2 + y^2 + (z+2.929)^2]\} + 1.40521y \exp\{-3.71756[x^2 + y^2 + (z+2.929)^2]\} \\
& - 0.614912y \exp\{-1.16545[x^2 + y^2 + (z-2.929)^2]\} + 0.614912y \exp\{-1.16545[x^2 + y^2 + (z+2.929)^2]\} \\
& - 0.111126y \exp\{-0.321892[x^2 + y^2 + (z-2.929)^2]\} + 0.111126y \exp\{-0.321892[x^2 + y^2 + (z+2.929)^2]\} \\
& + 0.0863376y(z-2.929) \exp\{-1.75[x^2 + y^2 + (z-2.929)^2]\} + 0.0863376y(z+2.929) \exp\{-1.75[x^2 + y^2 + (z+2.929)^2]\} \}
\end{aligned} \tag{A3}$$

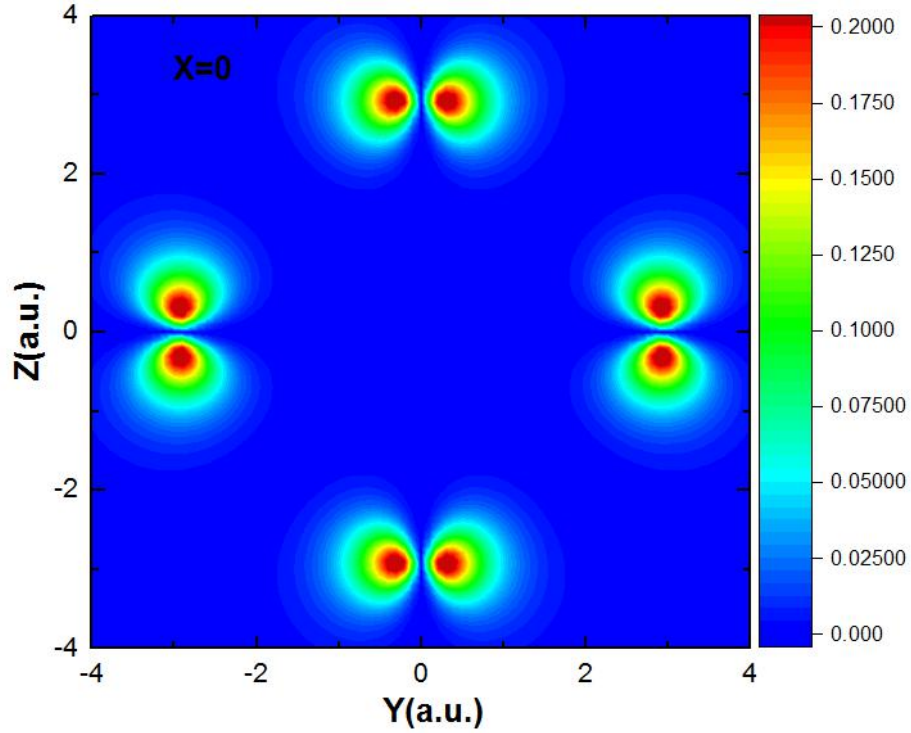


FIG. A3. The density distribution of wave function ψ'_3 with the value of $X=0$ a.u..

By the Fourier transform, the wave functions of ψ'_1 , ψ'_2 and ψ'_3 can be expressed in momentum space by ψ_1 , ψ_2 and ψ_3 , separately, which is

$$\begin{aligned}
\psi_1 = & \frac{1}{\sqrt{6482.2115}} [-0.0000274966p_y \sin(R_{SF}p_x) e^{-\frac{p^2}{221.764}} - 0.0011696p_y \sin(R_{SF}p_x) e^{-\frac{p^2}{50.5292}} \\
& -0.0186445p_y \sin(R_{SF}p_x) e^{\frac{p^2}{14.8702}} - 0.148263p_y \sin(R_{SF}p_x) e^{-\frac{p^2}{4.6618}} \\
& -0.668336p_y \sin(R_{SF}p_x) e^{-\frac{p^2}{1.28757}} + 0.00215274p_x p_y \cos(R_{SF}p_x) e^{-\frac{p^2}{7}} \\
& +0.0000274966p_x \sin(R_{SF}p_y) e^{-\frac{p^2}{221.764}} + 0.0011696p_x \sin(R_{SF}p_y) e^{-\frac{p^2}{50.5292}} \\
& +0.0186445p_x \sin(R_{SF}p_y) e^{\frac{p^2}{14.8702}} + 0.148263p_x \sin(R_{SF}p_y) e^{-\frac{p^2}{4.6618}} \\
& +0.668336p_x \sin(R_{SF}p_y) e^{-\frac{p^2}{1.28757}} - 0.00215274p_x p_y \cos(R_{SF}p_y) e^{-\frac{p^2}{7}}]
\end{aligned} \tag{A4}$$

$$\begin{aligned}
\psi_2 = & \frac{1}{\sqrt{6565.512}} [-0.0000274966p_z \sin(R_{SF}p_x) e^{-\frac{p^2}{221.764}} - 0.0011696p_z \sin(R_{SF}p_x) e^{-\frac{p^2}{50.5292}} \\
& -0.0186445p_z \sin(R_{SF}p_x) e^{\frac{p^2}{14.8702}} - 0.148263p_z \sin(R_{SF}p_x) e^{-\frac{p^2}{4.6618}} \\
& -0.668336p_z \sin(R_{SF}p_x) e^{-\frac{p^2}{1.28757}} + 0.00215274p_x p_z \cos(R_{SF}p_x) e^{-\frac{p^2}{7}} \\
& +0.0000274966p_x \sin(R_{SF}p_z) e^{-\frac{p^2}{221.764}} + 0.0011696p_x \sin(R_{SF}p_z) e^{-\frac{p^2}{50.5292}} \\
& +0.0186445p_x \sin(R_{SF}p_z) e^{\frac{p^2}{14.8702}} + 0.148263p_x \sin(R_{SF}p_z) e^{-\frac{p^2}{4.6618}} \\
& +0.668336p_x \sin(R_{SF}p_z) e^{-\frac{p^2}{1.28757}} - 0.00215274p_x p_z \cos(R_{SF}p_z) e^{-\frac{p^2}{7}}]
\end{aligned} \tag{A5}$$

and

$$\begin{aligned}
\psi_3 = & \frac{1}{\sqrt{6565.512}} [-0.0000274966p_z \sin(R_{SF}p_y) e^{-\frac{p^2}{221.764}} - 0.0011696p_z \sin(R_{SF}p_y) e^{-\frac{p^2}{50.5292}} \\
& -0.0186445p_z \sin(R_{SF}p_y) e^{\frac{p^2}{14.8702}} - 0.148263p_z \sin(R_{SF}p_y) e^{-\frac{p^2}{4.6618}} \\
& -0.668336p_z \sin(R_{SF}p_y) e^{-\frac{p^2}{1.28757}} + 0.00215274p_y p_z \cos(R_{SF}p_y) e^{-\frac{p^2}{7}} \\
& +0.0000274966p_y \sin(R_{SF}p_z) e^{-\frac{p^2}{221.764}} + 0.0011696p_y \sin(R_{SF}p_z) e^{-\frac{p^2}{50.5292}} \\
& +0.0186445p_y \sin(R_{SF}p_z) e^{\frac{p^2}{14.8702}} + 0.148263p_y \sin(R_{SF}p_z) e^{-\frac{p^2}{4.6618}} \\
& +0.668336p_y \sin(R_{SF}p_z) e^{-\frac{p^2}{1.28757}} - 0.00215274p_y p_z \cos(R_{SF}p_z) e^{-\frac{p^2}{7}}]
\end{aligned} \tag{A6}$$

Appendix B

We can obtain three wave functions for the HOMO-1 orbitals of SF₆ in momentum space in the following part, which is expressed as

$$\begin{aligned}
\psi_4 = & \frac{1}{\sqrt{6.0649141 \times 10^{12}}} \left\{ -ip_x (2.03526 \times 10^{-8} e^{-\frac{p^2}{1980.16}} + 9.4942 \times 10^{-7} e^{-\frac{p^2}{468.884}} + 0.0000169554 e^{-\frac{p^2}{151.1}} \right. \\
& + 0.00015655 e^{-\frac{p^2}{56.2336}} + 0.00093331 e^{-\frac{p^2}{22.263}} + 0.0020788 e^{-\frac{p^2}{9.05188}} \\
& - 0.0354173 e^{-\frac{p^2}{3.23198}} - 0.0175772 e^{-\frac{p^2}{1.10984}} + 0.467701 e^{-\frac{p^2}{0.308564}}) \\
& + i \sin(p_x R_{SF}) (1.24989 \times 10^{-9} e^{-\frac{p^2}{45708.4}} + 3.94247 \times 10^{-8} e^{-\frac{p^2}{6889.4}} \\
& + 5.88987 \times 10^{-7} e^{-\frac{p^2}{1582.98}} + 5.09161 \times 10^{-6} e^{-\frac{p^2}{460.556}} + 0.0000323751 e^{-\frac{p^2}{134.41}} \\
& + 0.0000695514 e^{-\frac{p^2}{19.676}} + 8.20719 \times 10^{-6} e^{-\frac{p^2}{221.776}} + 0.000200014 e^{-\frac{p^2}{50.5292}} \\
& - 1.837 \times 10^{-6} e^{-\frac{p^2}{14.8702}} - 0.0110525 e^{-\frac{p^2}{4.6618}} + 0.0826785 e^{-\frac{p^2}{1.28757}}) \\
& - ip_x \cos(p_x R_{SF}) (0.0000178434 e^{-\frac{p^2}{221.776}} + 0.00075904 e^{-\frac{p^2}{50.5292}} \\
& + 0.0120998 e^{-\frac{p^2}{14.8702}} + 0.104527 e^{-\frac{p^2}{4.6618}} + 0.487334 e^{-\frac{p^2}{1.28757}}) \\
& + i \sin(p_x R_{SF}) e^{-\frac{p^2}{7}} [-0.000569921(p_x^2 + p_y^2 - 2p_z^2) + 0.00170975(p_y^2 - p_x^2)] \\
& - ip_x \cos(p_y R_{SF}) (0.0000226208 e^{-\frac{p^2}{221.776}} + 0.000962267 e^{-\frac{p^2}{50.5292}} + 0.0153394 e^{-\frac{p^2}{14.8702}} \\
& + 0.121283 e^{-\frac{p^2}{4.6618}} + 0.543345 e^{-\frac{p^2}{1.28757}}) - 0.00167446 ip_x p_y \sin(p_y R_{SF}) e^{-\frac{p^2}{7}} \\
& - ip_x \cos(p_z R_{SF}) (0.0000226208 e^{-\frac{p^2}{221.776}} + 0.000962267 e^{-\frac{p^2}{50.5292}} + 0.0153394 e^{-\frac{p^2}{14.8702}} \\
& + 0.121283 e^{-\frac{p^2}{4.6618}} + 0.543345 e^{-\frac{p^2}{1.28757}} - 0.00167446 ip_x p_z \sin(p_z R_{SF}) e^{-\frac{p^2}{7}} \}
\end{aligned}
, \quad (B1)$$

$$\begin{aligned}
\psi_5 = & \frac{1}{\sqrt{6.0646892 \times 10^{12}}} \left\{ -ip_y (2.03526 \times 10^{-8} e^{-\frac{p^2}{1980.16}} + 9.4942 \times 10^{-7} e^{-\frac{p^2}{468.884}} + 0.0000169554 e^{-\frac{p^2}{151.1}} \right. \\
& + 0.00015655 e^{-\frac{p^2}{56.2336}} + 0.00093331 e^{-\frac{p^2}{22.263}} + 0.00207884 e^{-\frac{p^2}{9.05188}} \\
& - 0.0354173 e^{-\frac{p^2}{3.23198}} - 0.0175772 e^{-\frac{p^2}{1.10984}} + 0.467702 e^{-\frac{p^2}{0.308564}} \left. \right) \\
& + ip_y \cos(p_x R_{SF}) \left(-0.0000226208 e^{-\frac{p^2}{221.776}} + 0.000962267 e^{-\frac{p^2}{50.5292}} \right. \\
& + 0.0153394 e^{-\frac{p^2}{14.8702}} - 0.121283 e^{-\frac{p^2}{4.6618}} - 0.543345 e^{-\frac{p^2}{1.28757}} \left. \right) \\
& - 0.00221509i \sin(p_x R_{SF}) p_x p_y e^{-\frac{p^2}{7}} \\
& + i \sin(p_y R_{SF}) \left(1.24989 \times 10^9 e^{-\frac{p^2}{45708.4}} + 3.94247 \times 10^8 e^{-\frac{p^2}{6889.4}} \right. \\
& + 5.88987 \times 10^7 e^{-\frac{p^2}{1582.98}} + 5.09161 \times 10^6 e^{-\frac{p^2}{460.556}} + 0.0000323751 e^{-\frac{p^2}{134.41}} \\
& + 0.0000695514 e^{-\frac{p^2}{19.676}} + 8.20719 \times 10^6 e^{-\frac{p^2}{221.776}} + 0.000200014 e^{-\frac{p^2}{50.5292}} \\
& - 1.837 \times 10^6 e^{-\frac{p^2}{14.8702}} - 0.0110525 e^{-\frac{p^2}{4.6618}} + 0.0826785 e^{-\frac{p^2}{1.28757}} \left. \right) \\
& - ip_y \cos(p_y R_{SF}) \left(0.0000178434 e^{-\frac{p^2}{221.776}} + 0.000759064 e^{-\frac{p^2}{50.528}} \right. \\
& + 0.0120998 e^{-\frac{p^2}{14.8702}} + 0.104527 e^{-\frac{p^2}{4.6618}} + 0.487334 e^{-\frac{p^2}{1.28757}} \left. \right) \\
& - i \sin(p_y R_{SF}) (p_x^2 + p_y^2 - 2p_z^2) 0.000569921 e^{-\frac{p^2}{7}} \\
& - i \sin(p_y R_{SF}) (p_y^2 - p_x^2) 0.00170976 e^{-\frac{p^2}{7}} \\
& - ip_y \cos(p_z R_{SF}) \left(0.0000226208 e^{-\frac{p^2}{221.776}} + 0.000962267 e^{-\frac{p^2}{50.5292}} \right. \\
& + 0.0153394 e^{-\frac{p^2}{14.8702}} + 0.121283 e^{-\frac{p^2}{4.6618}} + 0.543345 e^{-\frac{p^2}{1.28757}} \left. \right) \\
& \left. - ip_y p_z \sin(p_z R_{SF}) 0.00167446 e^{-\frac{p^2}{7}} \right\}
\end{aligned}$$

, (B2)

and

$$\begin{aligned}
\psi_6 = & \frac{1}{\sqrt{6.0646707 \times 10^{12}}} \{ -ip_z (2.03526 \times 10^{-8} e^{-\frac{p^2}{1980.16}} + 9.4942 \times 10^{-7} e^{-\frac{p^2}{468.884}} + 0.0000169554 e^{-\frac{p^2}{151.1}} \\
& + 0.00015655 e^{-\frac{p^2}{56.2336}} + 0.00093331 e^{-\frac{p^2}{22.263}} + 0.00207884 e^{-\frac{p^2}{9.05188}} \\
& - 0.0354173 e^{-\frac{p^2}{3.23198}} - 0.0175772 e^{-\frac{p^2}{1.10984}} + 0.467702 e^{-\frac{p^2}{0.308564}}) \\
& - ip_z \cos(p_x R_{SF}) (0.0000226208 e^{-\frac{p^2}{221.776}} + 0.000962267 e^{-\frac{p^2}{50.5292}} \\
& + 0.0153394 e^{-\frac{p^2}{14.8702}} + 0.12183 e^{-\frac{p^2}{4.6618}} + 0.543345 e^{-\frac{p^2}{1.28757}}) \\
& - i \sin(p_x R_{SF}) p_x p_z 0.00167446 e^{-\frac{p^2}{7}} \\
& - ip_z \cos(p_y R_{SF}) (0.0000226208 e^{-\frac{p^2}{221.776}} + 0.000962267 e^{-\frac{p^2}{50.5292}} \\
& + 0.0153394 e^{-\frac{p^2}{14.8702}} + 0.121283 e^{-\frac{p^2}{4.6618}} + 0.543345 e^{-\frac{p^2}{1.28757}}) \\
& - ip_y p_z \sin(p_y R_{SF}) 0.00167446 e^{-\frac{p^2}{7}} \\
& + i \sin(p_z R_{SF}) (1.24989 \times 10^{-9} e^{-\frac{p^2}{45708.4}} + 3.94247 \times 10^{-8} e^{-\frac{p^2}{6889.4}} \\
& + 5.88987 \times 10^{-7} e^{-\frac{p^2}{1582.98}} + 5.09161 \times 10^{-6} e^{-\frac{p^2}{460.556}} + 0.0000323751 e^{-\frac{p^2}{134.41}} \\
& + 0.0000695514 e^{-\frac{p^2}{19.676}} + 8.20719 \times 10^{-6} e^{-\frac{p^2}{221.776}} + 0.000200014 e^{-\frac{p^2}{50.5292}} \\
& - 1.837 \times 10^{-6} e^{-\frac{p^2}{14.8702}} - 0.0110525 e^{-\frac{p^2}{4.6618}} + 0.0826785 e^{-\frac{p^2}{1.28757}}) \\
& - ip_z \cos(p_z R_{SF}) (0.0000178434 e^{-\frac{p^2}{221.776}} + 0.00075904 e^{-\frac{p^2}{50.5292}} \\
& + 0.0120998 e^{-\frac{p^2}{14.8702}} + 0.104527 e^{-\frac{p^2}{4.6618}} + 0.487334 e^{-\frac{p^2}{1.28757}}) \\
& + i \sin(p_z R_{SF}) (p_x^2 + p_y^2 - 2p_z^2) 0.00113979 e^{-\frac{p^2}{7}} \}
\end{aligned} \tag{B3}$$